

**Mechanisms affecting the transition from shallow to
deep convection over land: Inferences from
observations of the diurnal cycle collected at the
ARM Southern Great Plains site**

Yunyan Zhang* and Stephen A. Klein

Lawrence Livermore National Laboratory, Livermore, California, USA.

Journal of Atmospheric Sciences, Accepted on May 29, 2010

*Corresponding author: PCMDI, Atmospheric, Earth & Energy Division, Lawrence Livermore National Laboratory, Mail Code L-103, P.O. Box 808, Livermore, CA 94551 Email: zhang25@llnl.gov

ABSTRACT

11 years of summertime observations from the Atmospheric Radiation Measurement (ARM) Climate Research Facility Southern Great Plains (SGP) site are used to investigate mechanisms controlling the transition from shallow to deep convection over land. It is found that a more humid environment immediately above the boundary layer is present before the start of late-afternoon heavy precipitation events. The higher moisture content is brought by wind from the south. Greater boundary layer inhomogeneity in moist static energy, temperature, moisture and horizontal wind before precipitation begins is correlated to larger rain rates at the initial stage of precipitation. In an examination of afternoon rain statistics, higher relative humidity above the boundary layer is correlated to an earlier onset and longer duration of afternoon precipitation events, while greater boundary layer inhomogeneity and atmospheric instability in the 2 to 4 km layer above the surface are positively correlated to the total rain amount and the maximum rain rate. Although other interpretations may be possible, these observations are consistent with theories for the transition from shallow to deep convection that emphasize the role of a moist lower-free troposphere and boundary layer inhomogeneity.

1. Introduction

Convection and clouds are key processes that regulate the global energy and water budgets. The diurnal timing of convection is very important because the associated clouds strongly interact with both solar and infrared radiation. Numerous observations show that over land the diurnal maxima of deep convection and precipitation occur frequently in the late afternoon or early evening (Dai et al. 1999; Soden 2000; Dai 2001; Yang and Slingo 2001; Nesbitt and Zipser 2003). It is generally accepted that the diurnal variation over land is closely related to the solar heating of surface and atmospheric boundary layer, and thus is stronger in summertime.

Convection and clouds can not be explicitly simulated but are highly parameterized in conventional global climate models. The simulation of the diurnal cycle is an important measure of a climate model's performance (Randall et al. 1991; Yang and Slingo 2001; Tian et al. 2004; Dai 2006; Zhang et al. 2008). Traditional moist convection parameterizations are often associated with atmospheric instability in terms of convective available potential energy (CAPE) (Arakawa and Schubert 1974; Zhang and McFarlane 1995) or large-scale moisture convergence (Kuo 1965, 1974; Tiedtke 1989). A well-known problem is that climate models usually can not produce the observed afternoon convective rainfall peak over land (Dai et al. 1999; Yang and Slingo 2001); instead they usually simulate a quick onset of convective rainfall, before or at noon and in phase with the diurnal cycle of CAPE (Bechtold et al. 2004). Previous studies suggest that this deficiency is due to the lack of an intermediate stage involving shallow and middle-level topped cumulus and their associated effects, such as the gradual moistening of the free troposphere (Guichard et al. 2004). This reminds us that to solve this timing problem, we need to know what atmospheric conditions favor different convection regimes, such as shallow versus deep convection. In other words, what makes shallow cumulus stay shallow, and what promotes the transition of shallow to deep convection?

Recently studies of cloud resolving model (CRM) or large-eddy simulation (LES), in which fine-scale cloud processes can be explicitly resolved, have revealed several mechanisms on the transition from shallow to deep convection focusing on the influence of:

- Free tropospheric humidity, which influences the buoyancy of entraining cumulus clouds (Derbyshire et al. 2004; Kuang and Bretherton 2006).
- Sub-domain variability such as boundary layer cold pools driven by precipitation evaporation, which may promote further convection at gust front edges (Tompkins 2001; Chaboureau et al. 2004; Khairoutdinov and Randall 2006).
- Atmospheric instability at the cloud level when the transition from shallow to deep convection occurs (Houston and Niyogi 2007; Wu et al. 2009).

Considerable observational evidence also suggests that high values of lower tropospheric humidity precede deep convection especially over tropical oceans (Sherwood and Wahrlich 1999; Bretherton et al. 2004b; Mapes et al. 2006; Holloway and Neelin 2009). An association between the boundary layer inhomogeneity and deep convection has also been established from observations of stronger convection associated with squall lines (Wakimoto 1982), land-sea breezes (Kingsmill 1995) and mesoscale convective systems (Engerer and Stensrud 2008).

In this study, we use convective-regime-oriented composites from long-term observations over land to make a systematic assessment of these transition mechanisms. The Atmospheric Radiation Measurement (ARM, Strokes and Schwatz 1994; Ackerman and Stokes 2003) Climate Research Facility provides the necessary long-term comprehensive measurements at its Southern Great Plains (SGP) site. However, the coexistence of multiple convection regimes at various temporal and spatial scales complicates the analysis of SGP observations (Dong et al. 2005; Berg and Kassianov 2008). In order to assess theories for the transition, we are more interested in convection and clouds which are locally generated, limited in time to one diurnal cycle and not significantly influenced by large-scale forcing. Thus, the two regimes of interest to us are fair-weather non-precipitating shallow cumulus and late afternoon or early evening precipitating deep convection which, as will be shown below, grows from shallow convection. Our working hypothesis is that once an ensemble of observations is established for each of these regimes, the mechanisms affecting transition from shallow to deep convection would be revealed by comparing the statistics

of environmental parameters between and within convection regimes. If successful, a more typical composite case of each regime might be set up for future CRM, LES or single-column model (SCM) studies and provide information more relevant to the parameterization of convection in climate models. In this paper, we try to answer two questions:

(1) What environmental parameters differ between the two regimes, fair-weather shallow cumulus versus late afternoon deep convection, especially in the late morning a few hours before deep convection begins?

(2) Is there any correlation between environmental parameters and rain statistics on days with late-afternoon deep convection?

We expect that answers to these questions will provide useful inferences on the factors that favor the transition from shallow to deep convection. We also note that while our study is suitable for mid-latitude convection over land, our results might not apply to convection over other continental regions, such as the Amazon region with its dense vegetation coverage and stronger surface fluxes or coastal zones subject to the influence of land-sea breezes.

In the remaining parts of the paper, the observations and convection-regime classification are presented in section 2; the comparison between the two regimes is shown in section 3; the influence of environmental parameters on the rain statistics of late-afternoon deep convection is shown in section 4; discussions of transition mechanisms are presented in section 5; and conclusions including implications for convection parameterizations are discussed in section 6.

2. Data & Methodology

a. ARM Observations

The original data from ARM archive (<http://www.arm.gov/data>) are processed to hourly averages. Unless otherwise stated, measurements are taken at SGP central facility (CF) or in the region within a 50 km radius of the CF as shown in Figure 1. Specific data information is as follows:

- Precipitation from the Arkansas-Red Basin River Forecast Center (ABRFC, <http://www.arm.gov/data/vaps/abrfc>) is based on radar-observed precipitation estimates combined with rain gauge reports (Fulton et al. 1998; Breidenbach et al. 1998). We use the hourly-mean spatial average over the region within a 50 km radius of the CF.
- The vertical profile of cloud fraction is from Climate Modeling Best Estimate (CMBE, Xie et al. 2010, http://science.arm.gov/workinggroup/cpm/scm/best_estimate.html) Active Remote Sensing of CLOUDs data (ARSCL, Clothiaux et al. 2000, 2001, <http://science.arm.gov/vaps/arscl.stm>). The data are based on retrievals applied to measurements made by the vertical pointing millimeter wavelength cloud radar, micropulse lidar and laser ceilometers at the CF.
- Sounding data at the CF are from balloon sonde profiles whose water vapor is scaled with column-integrated precipitable water vapor retrieved from the microwave radiometer (Turner et al. 1998, <http://science.arm.gov/vaps/lssonde.stm>). Since the vertical resolution varies with meteorological conditions, data are re-gridded into a uniform resolution of 20 meters to facilitate composite analysis.
- Column-integrated precipitable water vapor (PWV) and liquid water path (LWP) are from CMBE Microwave Radiometer RETrievals (MWRRET, Turner et al. 2007, <http://science.arm.gov/vaps/mwrret.stm>).
- Surface sensible and latent heat fluxes are from the Bulk Aerodynamic Energy Balance Bowen Ratio data product (BAEBBR, Wesely et al. 1995, <http://science.arm.gov/vaps/baebbr.stm>) retrieved from measurements of an EBBR station at the CF.
- Surface temperature, moisture and winds are from the Surface Meteorological Observation Station (SMOS, <http://www.arm.gov/instruments/smos>) at the CF and four surrounding Oklahoma Mesonet (OKM, Brock et al. 1995, <http://www.arm.gov/instruments/okm>) stations shown in Figure 1.

- Large-scale wind fields are from the National Centers for Environmental Prediction Model Output Location Time Series (NCEP MOLTS, <http://www.arm.gov/instruments/molts>) data. They are provided by the Early Eta Model and its associated Eta Data Assimilation System.

We use the latest versions of value-added products to minimize the influence of measurement uncertainties. Forming a multi-day composite also significantly reduces the impact of random errors contained in an individual observation.

b. Warm-Season Convection Regime Classification

Figure 2 shows the average diurnal cycle for 1176 days with valid observations of cloud fraction and surface precipitation rate from May to August in the years 1997 to 2007. The precipitation rate has a primary peak between 0200 and 0300 local standard time (LST) and a secondary peak between 1800 and 1900 LST. A similar diurnal behavior is found for the number of days with hourly precipitation rate in excess of 1 mm day^{-1} . High clouds tend to occur between late afternoon and the following noon with a maximum of about 22% at 11 km in late evening. Low clouds, usually about 10 to 12% under 3 km, prefer to occur during daytime with a cloud base and top that rises gradually.

This diurnal variation hints at contributions from different convection regimes. The primary precipitation rate maximum between midnight and dawn is associated with eastward propagating convection systems (Carbone et al. 2002; Jiang et al. 2006) initiated at the front-range of the Rocky Mountains on the preceding afternoon. On the other hand, the secondary precipitation rate maximum during late afternoon or early evening might be a response to local surface heating (Jiang et al. 2006). With these thoughts in mind, we classify diurnal cycles for four convection regimes as follows:

1. **Clear-sky day.** The precipitation rate = 0 at all hours of the day and cloud fraction $\leq 5\%$ at all levels between 0800 and 1600 LST. A single day is defined as the time between 2 successive local midnights.

2. **Fair-weather non-precipitating shallow cumulus day.** The precipitation rate = 0 at all hours of the day, and shallow cumulus clouds are identified by Berg and Kassianov (2008) who first selected cumulus clouds based on fine temporal resolution ARSCL data at ARM SGP, and then manually scrutinized cloud images taken by the Total Sky Imager (<http://www.arm.gov/-instruments/tsi>) to eliminate low-cloud types other than shallow cumulus.
3. **Late afternoon or early evening deep convection day.** The diurnal maximum hourly precipitation rate $\geq 1 \text{ mm day}^{-1}$, occurs between 1500 and 2000 LST, and is at least twice more than the precipitation rate at any other hour of the day outside of 1500 to 2000 LST.
4. **Nighttime deep convection day.** The diurnal maximum hourly precipitation rate $\geq 1 \text{ mm day}^{-1}$ and occurs between midnight and 0700 LST.

There are 90, 95, 79 and 229 days for regimes 1 to 4, respectively with no overlap. The number of days in the four regimes do not sum to the total days with valid observations because there are other situations such as days with no precipitation but with clouds other than fair-weather shallow cumulus, days with drizzle, and days with heavy precipitation at hours which do not satisfy our criteria for late-afternoon nor nighttime deep convection. For the ensemble of late-afternoon deep convection days, our selection criteria selects many short duration rain events generated within 50 km of the CF as we desire, however they do not exclude the possibility of organized convection or large-scale forcing beyond the 50 km scope which we do not want to include. We examined animations of satellite infrared brightness temperature images provided by P. Minnis's group at the NASA Langley Center (<http://www-angler.larc.nasa.gov/>) for days with late-afternoon deep convection. A subjective judgment suggests that 15 days likely have features of convection organization or significant influence from large-scale forcing. Sensitivity tests show that the following results are not greatly affected if these days were omitted. As a result, we do not omit these days from the analysis in order to boost the sample size and statistical significance of the results.

Figure 3 shows the diurnal composites of precipitation and cloud fraction for regimes 1 to 4. On late afternoon deep convection days, precipitation starts from earlier afternoon, peaks at

about 21 mm day^{-1} at 1630 LST and diminishes after 2100 LST. On nighttime deep convection days, precipitation begins from preceding afternoon, peaks at about 30 mm day^{-1} at 0200 LST and lasts until early morning. On fair-weather shallow cumulus days, low cloud fraction maximizes at about 10 to 12% at 1.8 km from 1200 to 1400 LST. On late afternoon deep convection days, low cloud development is also found from early morning (0700 LST) to early afternoon (1400 LST), and more middle and high level clouds are present during these hours. On these days, the low cloud base gradually rises and the low cloud fraction maximizes at about 25% at 1.8 km near 1200 LST. After 1500 LST, deep convection clouds develop and peak at about 30% at 12 km between 1700 and 1800 LST and then high anvil clouds persist until midnight. Low clouds precede deep convection clouds on late afternoon deep convection days, while on the contrary, high clouds precede the deep convection clouds on nighttime deep convection days and are present during the whole precipitation process. This progression of clouds on nighttime deep convection days is consistent with propagating convection that is not locally generated.

3. Comparing Days of Fair-weather Shallow Cumulus with Days of Late-Afternoon Deep Convection

As revealed by the composites, shallow cumulus clouds are present on both fair weather and late-afternoon deep convection days. By contrasting the differences in environmental parameters between these two regimes, we hope to infer what factors cause shallow convection to remain shallow on some days, and to grow into deep convection on the other days. The differences between the two regimes are identified by comparing the composite mean of environmental parameters and its standard error which is defined as the standard deviation divided by the square root of the number of observations. We then make a 2-sided student t-test to identify which environmental parameters are the most distinguishable between the two regimes especially around 1130 LST, the nearest sounding time before deep convection occurs.

Since balloon soundings at 1130 LST are not available everyday, there are only 33 days with sounding data for late-afternoon deep convection and 69 days for fair-weather shallow cumulus. For the t-test and correlation calculations reported in the next section, only data for all parameters on valid sounding days are used and the result is considered statistically significant only if the null hypothesis can be rejected at the 95% confidence level.

a. Atmospheric Stability: CAPE and CIN

Figure 4 shows sounding composites in the lowest 4 km for potential temperature (θ) and water vapor mixing ratio at four local times: 0530, 1130, 1730 and 2330. In general, a stable boundary layer is found at 0530 LST. On shallow cumulus days, a well-mixed layer is found at 1130 LST and by 1730 LST the mixed-layer has deepened, warmed and dried. At 1130 LST, deep convection days tend to have a shallower mixed-layer and are slightly cooler and substantially moister than shallow cumulus days. At 1730 LST, there is a lack of well-mixedness on deep convection days which may result from the effects of precipitation on the sub-cloud layer. By 2330 LST, the boundary layer has returned to stable conditions for both regimes. Above 4 km, the temperature profiles of the two regimes are nearly identical (not shown), however, the mixing ratio tends to be higher on deep convection days; for example, at 4 km at 1130 LST it is 3.5 g kg^{-1} on deep convection days which is 1 g kg^{-1} larger than that on shallow cumulus days.

The composite soundings are used to investigate atmospheric stability. Figure 4 shows the virtual temperature differences ($T_{v,d}$) between the environmental sounding and a parcel of air raised from the boundary layer. $T_{v,d}$ is calculated by lifting an air parcel with the maximum equivalent potential temperature (θ_e) between 100 and 500 meters above ground through reversible adiabatic processes without mixing with the environment. $T_{v,d} > 0$ denotes positive buoyancy for the air parcel. Figure 4 shows a significant difference in the depth of Convection INhibition (CIN) layer between the two regimes. At 1130 LST, the Level of Free Convection (LFC) for shallow cumulus days is at 4.2 km while the LFC for deep convection days is at 2.5 km. The values of CAPE

and CIN are 700 J kg^{-1} and 40 J kg^{-1} , respectively, on deep convection days but 200 J kg^{-1} and 70 J kg^{-1} on shallow cumulus days. At 1730 LST, there is a slight decrease from the value at 1130 LST in CIN and a large increase in CAPE on shallow cumulus days while on deep convection days, both CIN and CAPE slightly increase from 1130 LST to 1730 LST.

b. Atmospheric humidity and liquid water content

Figure 5 shows the composite sounding of relative humidity (RH) at 1130 LST and the diurnal variation of the composite precipitable water vapor (PWV) and liquid water path (LWP) retrieved from the microwave radiometer. The sounding data show that more moisture is present on late-afternoon deep convection days in both the boundary layer and the free troposphere. Specifically RH is about 10% greater on deep convection days with the largest RH differences between 2 and 4 km. Note that the majority of shallow cumulus is beneath the 2.5 km level at 1130 LST for both regimes, indicating that the extra moisture in this layer is unlikely to be the result of moistening by cumulus clouds on the same day. The moisture difference is also apparent in PWV and LWP, both of which are significantly larger on days with afternoon deep convection. The PWV shows a strong diurnal cycle with an increase of about 5 mm from sunrise to its afternoon maximum. This average increase is larger than the average accumulated evaporation minus precipitation from the surface, suggesting that there is horizontal convergence of water vapor on days with afternoon deep convection. The afternoon peak of LWP of 110 g m^{-2} is in phase with the peak precipitation at 1730 LST while the peak LWP on shallow cumulus days is 15 g m^{-2} at 1330 LST.

c. Surface turbulent fluxes

Figure 6 shows that the diurnal composites of surface sensible and latent heat fluxes are in phase with the solar radiation. As the diurnal variation in surface heat fluxes drives the growth of the boundary layer, one might expect that greater surface fluxes would favor an increased chance of deep convection. However, surface heat fluxes on deep convection days are lower than that

on shallow cumulus days, particularly the latent heat flux. The reduced latent heat flux may be a response to boundary layer moisture. Specifically, the increase in near surface relative humidity from 45% on shallow cumulus days to 55% on deep convection days at 1130 LST (Figure 5) reduces the potential for evaporation and transpiration on deep convection days. The sensible heat fluxes are only distinguishable between 1330 LST till 1800 LST; the lower value on days with afternoon deep convection may be related to the reduced solar radiative heating of the surface (not shown). We also note that this association of reduced surface fluxes with deep convection may be similar to that found over tropical oceans as deep convection there is usually associated with moisture convergence and a minimum in surface fluxes (Sobel 2003).

d. Boundary layer inhomogeneity

To investigate boundary layer inhomogeneity, we use surface wind, temperature and humidity data measured by the SMOS at the central facility and four surrounding Oklahoma Mesonet stations (Figure 1).

Figure 7 shows the diurnal cycle of the mean and standard deviation (std dev) of the surface moist static energy (MSE), temperature, water vapor mixing ratio and horizontal wind speed across the five stations. The mesoscale wind (wind std dev) is defined as $\sqrt{u'^2 + v'^2}$, where u' and v' are the deviations in zonal and meridional wind from the 5-station mean. Note that we feel justified using the term mesoscale to define variability across the domain as the individual data at each station are 60-minute averages which correspond to a distance of 18 km for a 5 ms^{-1} horizontal wind speed. The mean MSE on deep convection days peaks in early afternoon around 1400 LST while that on shallow cumulus days maximizes in the last morning around 1100 LST. For both regimes, a quick increase of mixing ratio occurs in the early morning from 0600 to 0900 LST. After 0900 LST, the moisture on deep convection days stabilizes while the moisture on shallow cumulus days markedly decreases until sunset. The mean temperature difference is distinguishable between regimes only in the late afternoon and early evening. The mean daytime surface wind

speed on shallow cumulus days is slightly larger than that on deep convection days.

The variations in MSE, mixing ratio and wind speed across the domain become significantly larger on deep convection days after 1330 LST when precipitation starts to pick up. Although temperature variability is already larger on the morning of deep convection days, its significant increase occurs after 1330 LST. Broadly speaking, the station data clearly show that boundary layer inhomogeneity is significantly larger on deep convection days from near precipitation onset through early evening and beyond.

e. Large-scale wind fields

Figure 8 shows composites of horizontal and vertical winds from NCEP MOLTS data. Beneath 850 hPa, the horizontal wind fields are quite similar for both regimes. The wind direction is southwesterly before noon and turns to southeasterly in the afternoon and evening. Southerly winds prevail and become stronger during nighttime consistent with the existence of a low-level jet (Stensrud 1996).

The differences in horizontal winds between the two regimes are found at higher levels. Southerly winds extend into the middle and upper troposphere on deep convection days while the southerly component of the wind is near zero on shallow cumulus days especially during daytime. Though the westerly component of upper-level winds are stronger on deep convection days, the differences in westerly winds between the two regimes at middle and low levels are not large. The southerly winds immediately above the boundary layer on deep convection days could bring moister air from southerly locations leading to the greater humidity above the boundary layer.

To explore this idea, we correlate wind data at levels between 600 and 850 hPa with precipitable water vapor (PWV) from MWRRET. PWV varies with wind direction in the 600 to 850 hPa layer, as PWV with southerly winds is 20% higher than it is with northerly winds; while PWV does not differentiate between easterly and westerly winds. Although 60% of shallow cumulus days have southerly winds in the 600 to 850 hPa layer around 1130 LST, more than 80% of deep convection

days have southerly winds in this layer. However the magnitude of southerly winds does not seem to matter, as no significant correlation is found between the meridional wind in the 600 and 850 hPa layer and PWV. This suggests wind direction, rather than its speed, is more important for moisture in this layer.

With respect to large-scale vertical velocity, subsidence is found between 200 and 850 hPa on shallow cumulus days with an early-afternoon maximum. Subsidence is also present around 600 hPa from 0900 to 1500 LST on late-afternoon deep convection days, however with much reduced magnitude. In general, the subsidence is greatly reduced at all levels on deep convection days relative to that on shallow cumulus days.

f. What is the most different?

Figure 9 records t-values and significance levels for a set of environmental parameters at 1130 LST in the order of a decreasing t-value. Note that we examined differences at this time because this is the nearest time before the transition when soundings are available and because values of environmental parameters before the transition may indicate which factors are important for the transition.

The definitions of various environmental parameters are as follows. RH is calculated as the ratio of actual PWV to saturated PWV between 2 and 4 km and in the mixed layer. The NCEP winds are calculated between levels of 600 and 850 hPa, roughly corresponding to 1.2 to 4 km above ground level. These levels are examined because they correspond to CIN layers suggested by Figure 4. $-dT/dz$ is the temperature lapse rate between 2 and 4 km. CAPE and CIN are calculated from sounding profiles of temperature and humidity at 1130 LST. For an individual sounding, the buoyancy profile ($T_{v,d}$ in Figure 4) might cross the zero line several times. Because such complexity might lead to ambiguity in determining CAPE and CIN, we introduce an additional buoyancy parameter, the average undilute buoyancy regardless of sign below 5 km, to roughly measure the ability of a boundary layer air parcel originating from the mixed layer to reach the level

of free convection. Other environmental parameters are averages between 1030 and 1230 LST.

The results indicate the RH between 2 and 4 km at 1130 LST has the greatest statistical significance of all these environmental parameters. This supports the role of free-tropospheric humidity in influencing the transition from shallow cumulus to deep convection. Smaller latent heat flux and stronger 600-850 hPa southerly wind hints that moisture may be not only from surface evaporation and that southerly winds play an important role in moisture transfer into SGP region. At 1130 LST, a larger temperature standard deviation is found on deep convection days while the difference in MSE and moisture standard deviations are not significant. The differences in these standard deviations are significant at later hours of the day. CAPE and CIN are not significantly different between the two regimes at the 95% confidence level, which is possibly due to the noise introduced by the complexity of buoyancy profiles in individual soundings. However other measures of stability such as average buoyancy below 5 km and 2-4 km $-dT/dz$ are found to be significantly larger on deep convection days.

4. Comparing Afternoon Rain Statistics with Environmental Parameters

An alternate technique to determine the factors that favor the transition is to examine how rain statistics vary with environmental parameters only on the days with late afternoon deep convection. In particular, we ask: Is there any correlation between environmental parameters and rain statistics on days with late-afternoon deep convection? The rain statistics consist of four characteristics: total rain amount, the maximum hourly rain rate, the duration of a rain event, and the precipitation onset time. The onset time is defined as when the precipitation rate first exceeds zero mm day^{-1} at or after 1130 LST. Test of the onset time with the precipitation rate first exceeding 1 mm day^{-1} also yields similar results.

a. What is best correlated to afternoon rain?

Table 1 displays the correlation coefficients between afternoon rain statistics and environmental parameters at 1130 LST. The results indicate that larger RH between 2 to 4 km leads to earlier onset time and longer duration of precipitation. Total rain amount and maximum rain rate are positively correlated with the lapse rate between 2 and 4 km, boundary layer inhomogeneity in wind, temperature and humidity, and 600 to 850 hPa westerly wind. While the signs of these significant correlation coefficients match expectations, some parameters are correlated to the rain statistics in a way contrary to expectation. For example, larger CAPE is correlated with a later onset time and shorter duration of precipitation. A larger surface latent heat flux is related to a shorter duration of precipitation, which hints that the flux is a response to a drier boundary layer.

We note that some environmental parameters show no statistically significant correlation with the rain statistics though they are found significantly different between the two regimes in the t-test. These include mixed-layer RH, the magnitude of the southerly wind component between 600 and 850 hPa, the average buoyancy below 5 km of an undilute surface air parcel, and large-scale vertical velocity. Furthermore, some environmental parameters are correlated with the rain statistics even though they are not different significantly in the t-test. These include CAPE and boundary layer variability in MSE, mixing ratio and wind speed. These facts remind us that there might be limitations in both the t-test and this correlation test. For example, the results are sensitive to the choices of the measures, as CAPE, CIN, average buoyancy below 5 km and 2-4 km $-dT/dz$ each represent different aspects of atmospheric stability and show different behavior in the tests. Furthermore, the convection process is nonlinear and might be sensitive to a threshold value in some environmental parameters. As long as above a threshold, deep convection would be triggered and the actual magnitude of the environmental parameters might not be as important. In addition, as deep convection might occur sooner or later in the afternoon, using a fixed sounding time at 1130 LST might mix some signals in the environmental parameters at different stages relative to the triggering of convection. More detailed checks on the relationships in Table 1 are discussed in the following subsections.

Cross-correlation among environmental parameters are examined to identify redundant environmental parameters (not shown). The surprising correlation of rain statistics to the westerly wind between 600 and 850 hPa is partially explained by the fact that the westerly wind is positively correlated to both 2 to 4 km lapse rate and boundary layer temperature variability. Furthermore the fact that both 2 to 4 km RH and boundary layer moisture variability are positively related to (albeit different) rain statistics in Table 1 is striking given that greater 2 to 4 km RH is correlated significantly with smaller boundary layer moisture variability. Other environmental parameters have no significant correlations among each other and thus appear to be potentially independent predictors of afternoon rain statistics.

b. The relationship of sounding parameters to afternoon rain statistics

To provide an illustration of these relationships, we present Figure 10 which stratifies the rain statistics according to the two 1130 LST sounding parameters, 2 to 4 km RH and $-dT/dz$, which show the strongest relationship to afternoon rain. The 33 soundings at 1130 LST are sorted into 3 groups of 11 according to whether they have low, medium or high values of the sounding parameter. The mean and the standard error of each rain statistic are calculated from the 11 samples in each group. Figure 10 shows that total rain amount and maximum rain rate do not distinguish among different 2 to 4 km RHs. However with larger RH, the rain tends to start earlier and last longer. The quicker onset with larger RH is in agreement with Kuang and Bretherton (2006) who found in their LES that the transition is accelerated by a more humid free troposphere. The analysis for the 2 to 4 km temperature lapse rate ($-dT/dz$) shows that more unstable conditions are associated with larger total rain amount and maximum rain rate. Surprisingly, more unstable conditions are associated with a later precipitation onset time, contrary to the modeling results of Wu et al. (2009) and Houston and Niyogi (2007).

c. The relationship of boundary layer inhomogeneity to afternoon rain statistics

Because of its hourly record, our analysis of the relationship of rain statistics to boundary layer inhomogeneity need not be restricted to the values at 1130 LST. Furthermore, because boundary layer inhomogeneity can be both the cause and result of deep convection, high frequency data are necessary to discern cause and effect. To this end, we calculate the time-lag correlation coefficients between boundary layer inhomogeneity and the hourly precipitation rate. In performing this calculation, we align the time series data for each precipitation event with respect to the precipitation onset time. By so doing, we try to avoid mixing different development stages of deep convection.

Our results are illustrated with the matrix of lead-lag correlation coefficients in time relative to precipitation onset (Figure 11). The simultaneous correlation between inhomogeneity and precipitation is shown on the diagonal line (black solid line in Figure 11); the correlation coefficients for inhomogeneity leading (following) precipitation are shown in the lower-right (upper-left) part of the plot. For example, the correlation coefficient of moist static energy std dev 2 hours before precipitation begins with the precipitation rate 2 hours after precipitation begins is plotted at abscissa and ordinate location (2,-2) in Figure 11a.

The most significant correlations of precipitation appear with temperature variability and mesoscale wind speeds. Particularly prominent is a correlation coefficient of 0.7, the highest reported in this paper, between temperature variability and precipitation 3 hours after precipitation onset. The fact that the strongest correlations are along the diagonal line suggests that the time scale for precipitation to create boundary layer variability or vice versa must be fast and less than an hour. Although cause and effect may therefore be difficult to discern even with hourly data, a closer inspection of Figure 11b shows that during the first two hours after precipitation onset, the strongest correlation in each column is for precipitation leading temperature or wind variability by one hour. This hints that temperature or wind variability is the result of precipitation, at least early in a precipitation event.

The opposite relationship is suggested by the correlation at a level of 0.4 between the surface moisture variability 1 to 3 hours *before* the onset of precipitation and the precipitation rate 1 to 3

hours *after* the onset. This hints that surface moisture variability leads and therefore might enhance precipitation during the initial stage of a rain event.

5. Discussion

The calculations of sections 3 and 4 both suggest that lower tropospheric humidity and boundary layer inhomogeneity play important roles in the transition from shallow to deep convection. In this section, we use a Paluch diagram (Figure 12) for conservative thermodynamic variables (Paluch 1979; Neggers et al. 2002; Wu et al. 2009) to provide an interpretation of our results. In this diagram, an air parcel will preserve its thermodynamic properties (total water mixing ratio q_t and liquid water potential temperature θ_l) if it is lifted adiabatically without mixing with its environment. The properties of mixtures of boundary layer and environmental air would fall along the mixing line that connects the original air parcel properties in boundary layer with the properties of the environment at our chosen level. We select 2.5 km for this level as it is the level of free convection on deep convection days (Figure 4).

Figure 12 shows that on deep convection days at 1130 LST, almost all cloud properties including the average are negatively buoyant. The exception is for the undilute boundary layer air property which is barely positively buoyant. Thus is consistent with the fact that deep convection has not begun at 1130 LST. Since we do not have soundings at 1430 LST which is the mean time of transition to deep convection, we can only estimate the change in boundary layer air property based upon the changes in surface temperature and moisture in Figure 7 and with the assumption that the change in air properties at 2.5 km is small based on Figure 4. In this case, the undiluted boundary layer air is significantly positive buoyant and the average cloud property barely makes to zero-buoyancy line on deep convection days whereas the same quantities on shallow cumulus days are both negatively buoyant. Indeed it is striking that undiluted boundary layer air on shallow cumulus days is no closer to the zero buoyancy line at 1430 LST despite being 2 K warmer relative to the value at 1130 LST. This is due to the drying of the boundary layer in these three hours which

itself is likely the result of entrainment of relatively dry free tropospheric air into the boundary layer on these days.

It is also interesting to note that temperature differences between two regimes are small above the boundary layer (Figure 4). As a result, the difference between the two regimes in the zero-buoyancy lines decreases with height and is small relative to the separation between the two regimes in soundings and mixing lines. This means that it is the higher moisture both in and above the boundary layer that is the main reason leading to greater buoyancy on deep convection days for both an undilute air parcel and the average cloud property estimated from a mixing line.

Figure 12 also shows the possible values of boundary layer air properties at 1430 LST if the inhomogeneity in both temperature and moisture are considered based on Figure 7. Note that boundary layer inhomogeneity in Figure 7 represents mesoscale variability and thus is an underestimate of air parcel (~ 1 km) variability. It is obvious that in a certain range of combined variability in temperature and moisture, the buoyancy of an undilute air parcel or the average cloud property will increase positively. Furthermore, the Paluch diagram provides a means to understand why moisture variability may lead the precipitation by a few hours in the early stages of a precipitation event (Figure 11) and yet there is no distinguishable difference in moisture variability between shallow cumulus and deep convection days at 1130 LST (Figure 9). Specifically, the effect of a given temperature or moisture variability is larger on deep convection days than it is on shallow cumulus days because mixtures are closer to neutral buoyancy on deep convection days than they are on shallow cumulus days.

Nonetheless, the causes of boundary layer inhomogeneity before afternoon deep convection begins are unclear. Temperature variability at 1130 LST on deep convection days is 0.3 K larger than the variability on shallow cumulus days (Figure 7). One possibility is that the larger surface solar cloud radiative effect on deep convection days may induce greater mesoscale temperature variability. Note that the low cloud fraction on deep convection days is nearly double the value on shallow cumulus days (Figure 3).

Although thermodynamic conditions may explain the difference between regimes, one must

still ask: how does an air parcel reach the level of free convection? This leads us to consider the role of surface fluxes and boundary layer inhomogeneity in creating the momentum to overcome the CIN layer. Traditionally the vertical velocity of air parcel in the boundary layer can be characterized by the convective velocity scale, w_* , which we can calculate from the observed surface fluxes and mixed layer depth. We find that w_*^2 is about 1.4^2 J kg^{-1} for deep convection days and 1.7^2 J kg^{-1} for shallow cumulus days at 1130 LST. These kinetic energy values are small relevant to the CIN present at 1130 LST. However the CIN at transition time may be considerably smaller and mesoscale fluctuations in wind speed which are larger on deep convection days (Figure 7) may contribute additional momentum that could increase the chances for shallow cumulus to transit to deep convection.

6. Summary and Implications for Convection Parameterization

11 years of summertime observations at the ARM Southern Great Plains site have been used to categorize the diurnal cycle into different convection regimes based on the diurnal variation of precipitation and clouds. We focus on the comparison of environmental parameters between two regimes, the days with fair-weather shallow cumulus and the days with afternoon deep convection, in order to reveal the mechanisms controlling the transition from shallow to deep convection.

A few hours before rain events begin on afternoon deep convection days, higher relative humidity is found both in and above the boundary layer, especially between the levels of 2 to 4 km above the surface. The higher moisture content at 2 to 4 km depends on the wind direction being from south. Relative to days of fair-weather shallow cumulus, greater instability, stronger inhomogeneity in boundary layer temperature, less wind shear between 600 and 850 hPa, and weaker subsidence are found preceding afternoon rain events. Based on the composite sounding for the two regimes, we also find that the level of free convection is 1.7 km lower on days with afternoon rain events. Furthermore, although the diurnal variation in surface fluxes drives the growth of the boundary layer, the difference between regimes in their magnitude appears to be a response to

changed boundary layer conditions.

We then focused on the relationship between these conditions at 1130 LST and afternoon rain statistics. Four afternoon rain properties, the total rain amount, maximum hourly rain rate, rain onset time and duration of rain were investigated. With greater 2 to 4 km relative humidity, rain starts earlier and lasts longer. Boundary layer inhomogeneity, 600 to 850 hPa westerly wind component and the 2 to 4 km lapse rate are positively correlated with total rain and maximum rain rate; furthermore, these environmental parameters are correlated with each other.

While not manifest in every statistical test, these observations are consistent with a role for lower troposphere (2 to 4 km) humidity and boundary layer inhomogeneity in the transition from shallow to deep convection. This provides some observational support for the transition theories based upon LES and is consistent with previous observations which have focused mainly on tropical ocean deep convection. With respect to boundary layer variability, we showed that in the early stage of precipitation, boundary layer temperature and wind variability slightly lags precipitation by up to 1 hour (Figure 12b,d). The creation of cold pools by deep convection may explain this correlation as well as the large increase of boundary layer inhomogeneity on deep convection days relative to that on shallow cumulus days. In addition, we also showed a connection between moisture and moist static energy inhomogeneity before afternoon precipitation begins and the subsequent precipitation (Figure 12a,c and Table 1). This last correlation suggests that boundary layer inhomogeneity promotes as well as results from deep convection. Note, however, that the inhomogeneity which may promote convection is not due to cold pools as this is the inhomogeneity present before precipitation. The reason we do not observe cold pools promoting convection may be that this effect is masked by the more dominant effect of convection causing cold pools. To observe the effect of cold pools promoting convection may require alternate observational techniques such as a detailed analysis of individual events using the new scanning doppler cloud radars and lidars currently being installed by ARM at the Southern Great Plains site.

A plausible, albeit not exclusive, interpretation is that the observational evidence is consistent with a mechanistic view of the transition from shallow to deep convection that emphasizes the abil-

ity of a parcel of boundary layer air to reach the level of free convection. In particular, the parcels that reach the level of free convection are those that have the highest values of moisture in the boundary layer and they may have more momentum than expected due to mesoscale fluctuations in boundary layer wind. The ability of the “lucky” parcels to reach the level of free convection is also assisted by high relative humidity and a steeper lapse rate in the first few kilometers above the boundary layer. Higher relative humidity in this layer diminishes the buoyancy reducing effects of entrainment whereas the steeper lapse rate increases parcel buoyancy directly. Therefore, these observations provide partial support to parameterizations focusing on the ability of boundary layer air parcel to penetrate level of free convection, similar to the evolving CIN-based parameterizations of moist convection that have been under development for a number of years (Mapes 2000; Bretherton et al. 2004a; Fletcher and Bretherton 2009). Furthermore, the observations are somewhat encouraging for the nascent efforts to parametrize mesoscale boundary layer inhomogeneity (Rio et al. 2009) and its role in the transition from shallow to deep convection.

Acknowledgments.

The authors sincerely thank Larry Berg for providing the index for shallow cumulus days, Shaocheng Xie for providing codes to calculate CAPE and CIN, and Renata McCoy for discussions on the CMBE data. The authors thank Brian Mapes, Peter Caldwell and Shaocheng Xie for comments on the manuscript and Bjorn Stevens, Chris Bretherton and Robert Pincus for discussions. The authors also appreciate the comments of three anonymous reviewers which helped to improve the manuscript. The authors thank Department of Energy’s Atmospheric Radiation Measurement Climate Research Facility data archive and Oklahoma Mesonet data. This work was supported through the Department of Energy’s Atmospheric System Research Program which is directed from the Biological and Environmental Research program at the Office of Science. This work was performed under the auspices of the U.S. Department of Energy by Lawrence Livermore National Laboratory under Contract DE-AC52-07NA27344.

REFERENCES

- Ackerman, T. P. and G. M. Stokes, 2003: The Atmospheric Radiation Measurement program. *Physics Today*, **56**, 38–44.
- Arakawa, A. and W. H. Schubert, 1974: Interaction of a cumulus cloud ensemble with the large-scale environment, part I. *J. Atmos. Sci.*, **31**, 674–701.
- Bechtold, P., J.-P. Chaboureau, A. Beljaars, A. K. Betts, M. Köhler, M. Miller, and J.-L. Re-delsperger, 2004: The simulation of the diurnal cycle of convective precipitation over land in a global model. *Quart. J. Roy. Meteor. Soc.*, **130**, 3119–3137.
- Berg, L. K. and E. I. Kassianov, 2008: Temporal variability of fair-weather cumulus statistics at the acrf sgp site. *J. Climate*, **21**, 3344–3358.
- Breidenbach, J., D. J. Seo, and R. Fulton., 1998: Stage II and III post processing of NEXRAD precipitation estimates in the modernized weather service. *AMS 78th Annual Meeting*, Phoenix, Arizona.
- Bretherton, C. S., J. R. McCaa, and H. Grenier, 2004a: A new parameterization for shallow cumulus convection and its application to marine shallow subtropical cloud-topped boundary layers. part I: description and 1d results. *Mon. Wea. Rev.*, **132**, 864–882.
- Bretherton, C. S., M. E. Peters, and L. E. Back, 2004b: Relationships between water vapor path and precipitation over the tropical oceans. *J. Climate*, **17**, 1517–1528.
- Brock, F. V., K. C. Crawford, R. L. Elliott, G. W. Cuperus, S. J. Stadler, H. L. Johnson, and M. D. Eilts, 1995: The Oklahoma Mesonet: A technical overview. *J. Atmos. Oceanic Technol.*, **12**, 5–19.

- Carbone, R. E., J. D. Tuttle, D. A. Ahijevych, and S. B. Trier, 2002: Inferences of predictability associated with warm season precipitation episodes. *J. Atmos. Sci.*, **59**, 2033–2056.
- Chaboureau, J.-P., F. Guichard, J.-L. Redelsperger, and J.-P. Lafore, 2004: The role of stability and moisture in the diurnal cycle of convection over land. *Quart. J. Roy. Meteor. Soc.*, **130**, 3105–3117.
- Clothiaux, E., et al., 2001: *The ARM Millimeter Wave Cloud Radars (MMCRs) and the Active Remote Sensing of Clouds (ARSCL) Value Added Product (VAP)*. DOE Tech. Memo. ARM VAP-002.1, U.S. Department of Energy, Washington, D.C.
- Clothiaux, E. E., T. P. Ackerman, G. G. Mace, K. P. Moran, R. T. Marchand, M. Miller, and B. E. Martner, 2000: Objective determination of cloud heights and radar reflectivities using a combination of active remote sensors at the ARM CART sites. *J. Appl. Meteor.*, **39**, 645–665.
- Dai, A., 2001: Global precipitation and thunderstorm frequencies. Part II: Diurnal variations. *J. Climate*, **14**, 1112–1128.
- Dai, A., 2006: Precipitation characteristics in eighteen coupled climate models. *J. Climate*, **19**, 4605–4630.
- Dai, A., F. Giorgi, and K. Trenberth, 1999: Observed and model-simulated diurnal cycles of precipitation over the contiguous United States. *J. Geophys. Res.*, **104**, 6377–6402.
- Derbyshire, S. H., I. Beau, P. Bechtold, J.-Y. Grandpeix, J.-M. Piriou, J.-L. Redelsperger, and P. M. M. Soares, 2004: Sensitivity of moist convection to environmental humidity. *Quart. J. Roy. Meteor. Soc.*, **130**, 3055–3079.
- Dong, X., P. Minnis, and B. Xi, 2005: A climatology of midlatitude continental clouds from the arm sgp Central Facility. Part I: Low-level cloud macrophysical, microphysical and radiative properties. *J. Climate*, **18**, 1391–1410.

- Engerer, N. A. and D. J. Stensrud, 2008: Surface characteristics of observed cold pools. *Mon. Wea. Rev.*, **136**, 4839–4849.
- Fletcher, J. K. and C. S. Bretherton, 2009: Evaluating boundary-layer based mass-flux closures using cloud-resolving model simulations of deep convection. *J. Atmos. Sci.*, in review.
- Fulton, R., J. Breidenbach, D. Seo, D. Miller, and T. O'Connell, 1998: The WSR-88D rainfall algorithm. *Wea. Forecasting*, **13**, 377–395, DOI: 10.1175/1520-0434(1998)013<0377:TWRA>2.0.CO;2.
- Guichard, F., et al., 2004: Modeling the diurnal cycle of deep precipitating convection over land with cloud-resolving models and single-column models. *Quart. J. Roy. Meteor. Soc.*, **130**, 3139–3172.
- Holloway, C. and J. Neelin, 2009: Moisture vertical structure, column water vapor, and tropical deep convection. *J. Atmos. Sci.*, **66**, 1665–1683.
- Houston, A. L. and D. Niyogi, 2007: The sensitivity of convective initiation to the lapse rate of the active cloud-bearing layer. *Mon. Wea. Rev.*, **135**, 3013–3032.
- Jiang, X., N.-C. Lau, and S. A. Klein, 2006: Role of eastward propagating convection systems in the diurnal cycle and seasonal mean of summertime rainfall over the u.s. great plains. *Geophys. Res. Lett.*, **33**, L19 809, doi:10.1029/2006GL027022.
- Khairoutdinov, M. F. and D. A. Randall, 2006: High-resolution simulation of shallow-to-deep convection transition over land. *J. Atmos. Sci.*, **63**, 3421–3436.
- Kingsmill, D. E., 1995: Convection initiation associated with a sea-breeze front, a gust front, and their collision. *Mon. Wea. Rev.*, **123**, 2913–2933.
- Kuang, Z. and C. S. Bretherton, 2006: A mass-flux scheme view of a high-resolution simulation of a transition from shallow to deep cumulus convection. *J. Atmos. Sci.*, **63**, 1895–1909.

- Kuo, H. L., 1965: On formation and intensification of tropical cyclones through latent heat release by cumulus convection. *J. Atmos. Sci.*, **22**, 40–63.
- Kuo, H. L., 1974: Further studies of the parameterization of the influence of cumulus convection on large-scale flow. *J. Atmos. Sci.*, **31**, 1232–1240.
- Mapes, B., S. Tulich, J. Lin, and P. Zuidema, 2006: The mesoscale convection life cycle: Building block or proto- type for large-scale tropical waves? *Dyn. Atmos. Ocean.*, **42**, 3–29.
- Mapes, B. E., 2000: Convective inhibition, subgrid-scale triggering energy, and stratiform instability in a toy tropical wave model. *J. Atmos. Sci.*, **57**, 1515–1535.
- Neggers, R. A. J., A. P. Siebesma, and H. J. J. Jonker, 2002: A multiparcel model for shallow cumulus convection. *J. Atmos. Sci.*, **59**, 1655–1668.
- Nesbitt, S. and E. J. Zipser, 2003: The diurnal cycle of rainfall and convective intensity according to three years of TRMM measurements. *J. Climate*, **16**, 1456–1475.
- Paluch, I. R., 1979: The entrainment of air in colorado cumuli. *J. Atmos. Sci.*, **36**, 2467–2478.
- Randall, D. A., Harshvardhan, and D. A. Dazlich, 1991: Diurnal variability of the hydrologic cycle in a general circulation model. *J. Atmos. Sci.*, **48**, 40–62.
- Rio, C., F. Hourdin, J. Grandpeix, and J. Lafore, 2009: Shifting the diurnal cycle of parameterized deep convection over land. *Geophys. Res. Lett.*, **36**, L07809, doi:10.1029/2008GL036779.
- Sherwood, S. C. and R. Wahrlich, 1999: Observed evolution of tropical deep convective events and their environment. *Mon. Wea. Rev.*, **127**, 1777–1795.
- Sobel, A., 2003: On the coexistence of an evaporation minimum and precipitation maximum in the warm pool. *J. Climate*, **16**, 1003–1009.
- Soden, B. J., 2000: The diurnal cycle of convection, clouds and water vapor in the tropical upper troposphere. *Geophys. Res. Lett.*, **27**, 2173–2176.

- Stensrud, D. J., 1996: Importance of low-level jets to climate: A review. *J. Climate*, **9**, 1698–1711.
- Strokes, G. M. and S. E. Schwatz, 1994: The Atmospheric Radiation Measurement (ARM) program: Programmatic background and design of the cloud and radiation test bed. *Bull. Amer. Meteor. Soc.*, **75**, 1201–1221.
- Tian, B., B. J. Soden, and X. Wu, 2004: Diurnal cycle of convection, clouds, and water vapor in the tropical upper troposphere: Satellites versus a general circulation model. *J. Geophys. Res.*, **109**, D10101, DOI:10.1029/2003JD004117.
- Tiedtke, M., 1989: A comprehensive mass flux scheme for cumulus parameterization in large-scale models. *Mon. Wea. Rev.*, **117**, 1779–1800.
- Tompkins, A. M., 2001: Organization of tropical convection in low vertical wind shears: the role of cold pools. *J. Atmos. Sci.*, **58**, 1650–1672.
- Turner, D., S. Clough, J. Liljegren, E. Clothiaux, K. Cady-Pereira, and K. Gaustad, 2007: Retrieving liquid water path and precipitable water vapor from Atmospheric Radiation Measurement (ARM) microwave radiometers. *IEEE Trans. Geosci. Remote Sens.*, **45**, 3680–3690, doi:10.1109/TGRS.2007.903703.
- Turner, D., T. Shippert, P. Brown, S. Clough, R. Knuteson, H. Revercomb, and W. Smith., 1998: Long-term analyses of observed and line-by-line calculations of longwave surface spectral radiance and the effect of scaling the water vapor profile. *In Proceedings of the Eighth Atmospheric Radiation Measurement Science Team Meeting*, Tucson, Arizona.
- Wakimoto, R. M., 1982: The life cycle of thunderstorm gust fronts as viewed with doppler radar and rawinsonde data. *Mon. Wea. Rev.*, **110**, 1060–1082.
- Wesely, M., D. Cook, and R. Coulter, 1995: Surface heat flux data from energy balance Bowen ratio systems. *Preprints of the 9th Symposium on Meteorological Observations and Instrumentation*, Charlotte, North Carolina, Amer. Meteorol. Soc., Boston Massachusetts, pp. 486-489.

- Wu, C., B. Stevens, and A. Arakawa, 2009: What controls the transition from shallow to deep convection? *J. Atmos. Sci.*, **66**, 1793–1806.
- Xie, S., et al., 2010: ARM climate modeling best estimate data. *Bull. Amer. Meteor. Soc.*, **91**, 10.1175/2009BAMS2891.1.
- Yang, G.-Y. and J. M. Slingo, 2001: The diurnal cycle in the tropics. *Mon. Wea. Rev.*, **129**, 784–801.
- Zhang, G. J. and N. A. McFarlane, 1995: Sensitivity of climate simulations to the parameterization of cumulus convection in the canadian climate centre general circulation model. *Atmos. Ocean*, **33**, 407–446.
- Zhang, Y., et al., 2008: On the diurnal cycle of deep convection, high-level cloud, and upper troposphere water vapor in the Multiscale Modeling Framework. *J. Geophys. Res.*, **113**, doi:10.1029/2008JD09905.

List of Figures

- 1 The map of ARM Facilities and Mesonet stations. Numbers denote the distance (km) between Mesonet stations. The circle encloses the area within 50 km of the ARM SGP central facility and over which precipitation data are averaged. 33
- 2 Averaged warm-season diurnal cycle of ABRFC surface precipitation (left) and CMBE ARSCL cloud fraction (right), for Mays to Augusts of years 1997 to 2007. The red line in the left plot denotes the hourly precipitation rate in mm day^{-1} . Black dots in the left plot denote the number of days in which the hourly precipitation rate is greater than 1 mm day^{-1} during a certain hour. The green shaded area in the left plot identifies the diurnal cycle of interest. The 9-hour period before and after is also shown for the purpose of process continuity. 34
- 3 Diurnal cycle composites of ABRFC surface precipitation (a) and CMBE ARSCL cloud fraction (b-e) for different convection regimes: clear-sky days (b); fair-weather shallow cumulus days (c); late afternoon deep convection days (d) and nighttime deep convection days (e). In (a), the blue line denotes the precipitation rate for late afternoon deep convection days; while the red line is for nighttime deep convection days. The green shaded area in (a) signifies the diurnal cycle of interest. The 9-hour period before and after is also shown for the purpose of process continuity. 35

4	Composite soundings for potential temperature (θ) and Mixing Ratio (MR) and the virtual temperature difference ($T_{v,d}$) between the environmental sounding and an air parcel lifted through reversible adiabatic processes from the boundary layer for fair-weather shallow cumulus days (dashed) and late-afternoon deep convection days (solid) at different Local Standard Times (LST).	36
5	Composite Relative Humidity (RH, a) at 1130 LST from sounding data and composite diurnal cycle of precipitable water vapor (PWV, b) and liquid water path (LWP, c) from CMBE MWRRET data. The width of the color shading on either side of the mean value denotes one standard error of the mean across all the sample days in each regime. The dashed line in panel b) is the PWV calculated based on the integral of evaporation and precipitation since 0530 LST for days with late-afternoon deep convection. Time-averaged LWP values are not conditioned on the presence of cloud and thus they are not in-cloud averages.	37
6	Diurnal cycle composite of surface sensible heat flux (a) and latent heat flux (b) from BAEBBR data for fair-weather shallow cumulus days and late-afternoon deep convection days. The width of the color shading on either side of the mean value denotes one standard error of the mean across all the sample days in each regime.	38

7	Diurnal cycle composite of mean surface Moist Static Energy (MSE, a), temperature (b), and Mixing Ratio (MR, c), and their standard deviations (std dev, d-f). Also shown are the mean surface wind speed (g) and the mesoscale wind speed (h). Mean and std dev values are calculated based on SMOS data at the SGP central facility and four nearby Oklahoma Mesonet stations. Mean MSE and its std dev are normalized by the heat capacity at constant pressure for dry air (C_{pd}), and thus are in units of K. The width of the color shading on either side of the mean value denotes one standard error of the mean value across all sample days in each regime.	39
8	Composite diurnal cycle of winds from the NCEP MOLTS data at SGP: zonal (left), meridional (middle) and vertical pressure wind (omega, right) for fair-weather shallow cumulus days (top) and late-afternoon deep convection days (bottom).	40
9	Absolute t-values from student t-tests for the differences between composite means of fair-weather shallow cumulus days and late-afternoon deep convection days around 1130 LST. The horizontal line denotes a confidence level of 95%. Negative (positive) t-values are in solid (stipple) pattern, and denote smaller (larger) composite means on deep convection days relative to the mean on fair-weather shallow cumulus days.	41
10	Afternoon rain statistics stratified according to low, medium and high values of Relative Humidity (RH) and lapse rate ($-dT/dz$) between 2 and 4 km at 1130 LST. The statistics include total afternoon rain (top), maximum hourly rain rate (second), duration of rain event (third), and precipitation onset time (bottom). The black dots indicate the mean values of precipitation statistics and the width of the black lines indicate two standard errors. The mean values for each of the three ranges of RH and lapse rate are displayed on the abscissa.	42

- 11 Lead-lag correlation coefficients between the precipitation rate of late-afternoon deep convection days and the standard deviation of surface Moist Static Energy (MSE) (a), surface temperature (b), surface Mixing Ratio (MR) (c) and mesoscale wind speed (d). The scale for both the abscissa and ordinate are hours after precipitation onset time. Only correlation coefficients that are significant at 95% confidence level and have been calculated from samples sizes greater than 30 are displayed. 43
- 12 Conservative variables diagram (Paluch diagram) of total water mixing ratio (q_t) and liquid water potential temperature (θ_l) for the composite of sounding data (gray circles) at 1130 LST for fair-weather shallow cumulus days (left) and late afternoon deep convection days (right). Dotted lines are the saturation curves and long-dashed lines are the zero-buoyancy lines calculated based on sounding data at 2.5 km. The black solid line connects the air properties in the boundary layer at 1130 LST (the black dot labeled “BL₁₁₃₀”) and at the level of 2.5 km (the black dot labeled “2.5 km”) and is the mixing line along which mixtures of air in boundary layer and the 2.5 km level would fall. The portion of the mixing line above the zero-buoyancy line indicates mixture is positively buoyant at 2.5 km. Above the saturation curve, the mixture is cloudy at 2.5 km. The black cross denotes the average property of the mixing line above the saturation curve which is an approximation to the average properties of the cloud at 2.5 km. The boundary layer air property at 1430 LST is denoted by black dot labeled “BL₁₄₃₀”. The stippled area denotes the possible values a boundary layer air parcel may have if boundary layer inhomogeneity is considered. This area encompasses one standard deviation of boundary layer inhomogeneity about the mean value (Figure 7). 44

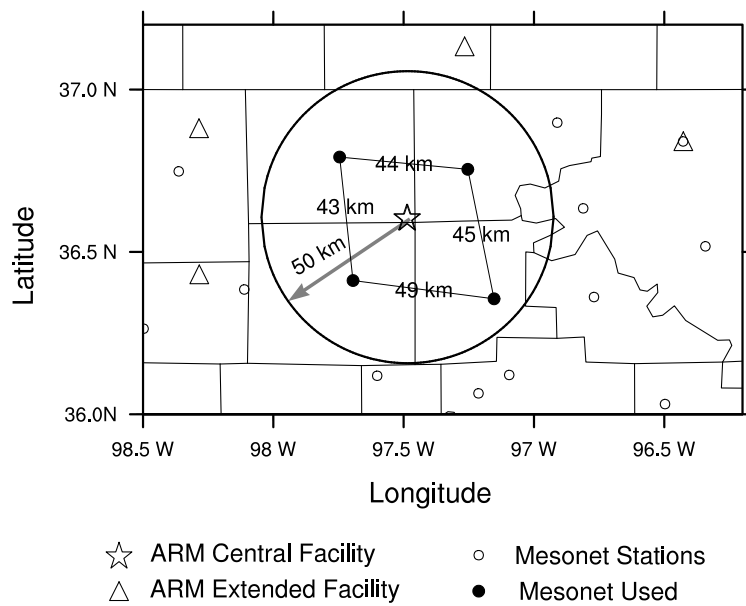


FIG. 1. The map of ARM Facilities and Mesonet stations. Numbers denote the distance (km) between Mesonet stations. The circle encloses the area within 50 km of the ARM SGP central facility and over which precipitation data are averaged.

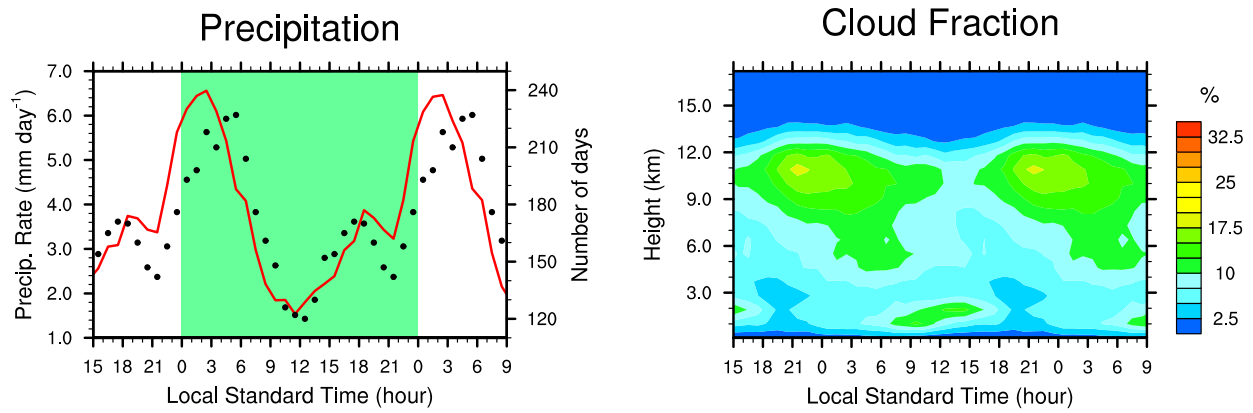


FIG. 2. Averaged warm-season diurnal cycle of ABRFC surface precipitation (left) and CMBE ARSCL cloud fraction (right), for Mays to Augusts of years 1997 to 2007. The red line in the left plot denotes the hourly precipitation rate in mm day^{-1} . Black dots in the left plot denote the number of days in which the hourly precipitation rate is greater than 1 mm day^{-1} during a certain hour. The green shaded area in the left plot identifies the diurnal cycle of interest. The 9-hour period before and after is also shown for the purpose of process continuity.

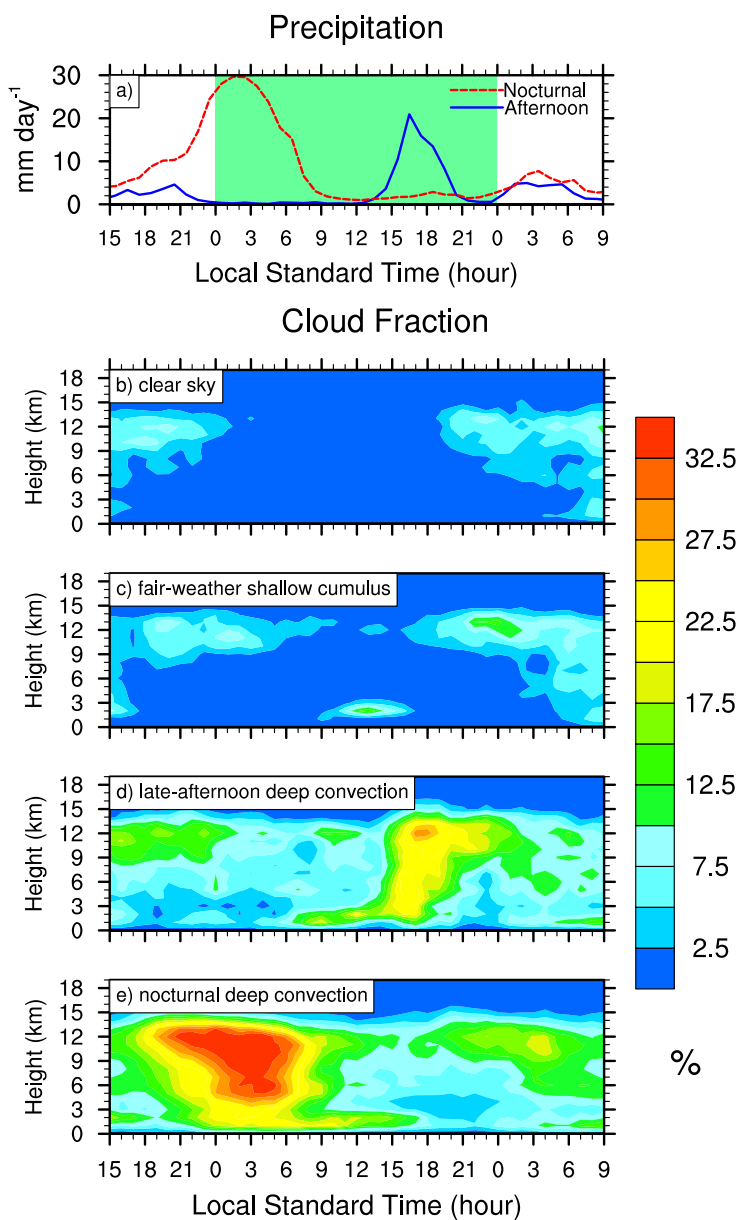


FIG. 3. Diurnal cycle composites of ABRFC surface precipitation (a) and CMBE ARSCL cloud fraction (b-e) for different convection regimes: clear-sky days (b); fair-weather shallow cumulus days (c); late afternoon deep convection days (d) and nighttime deep convection days (e). In (a), the blue line denotes the precipitation rate for late afternoon deep convection days; while the red line is for nighttime deep convection days. The green shaded area in (a) signifies the diurnal cycle of interest. The 9-hour period before and after is also shown for the purpose of process continuity.

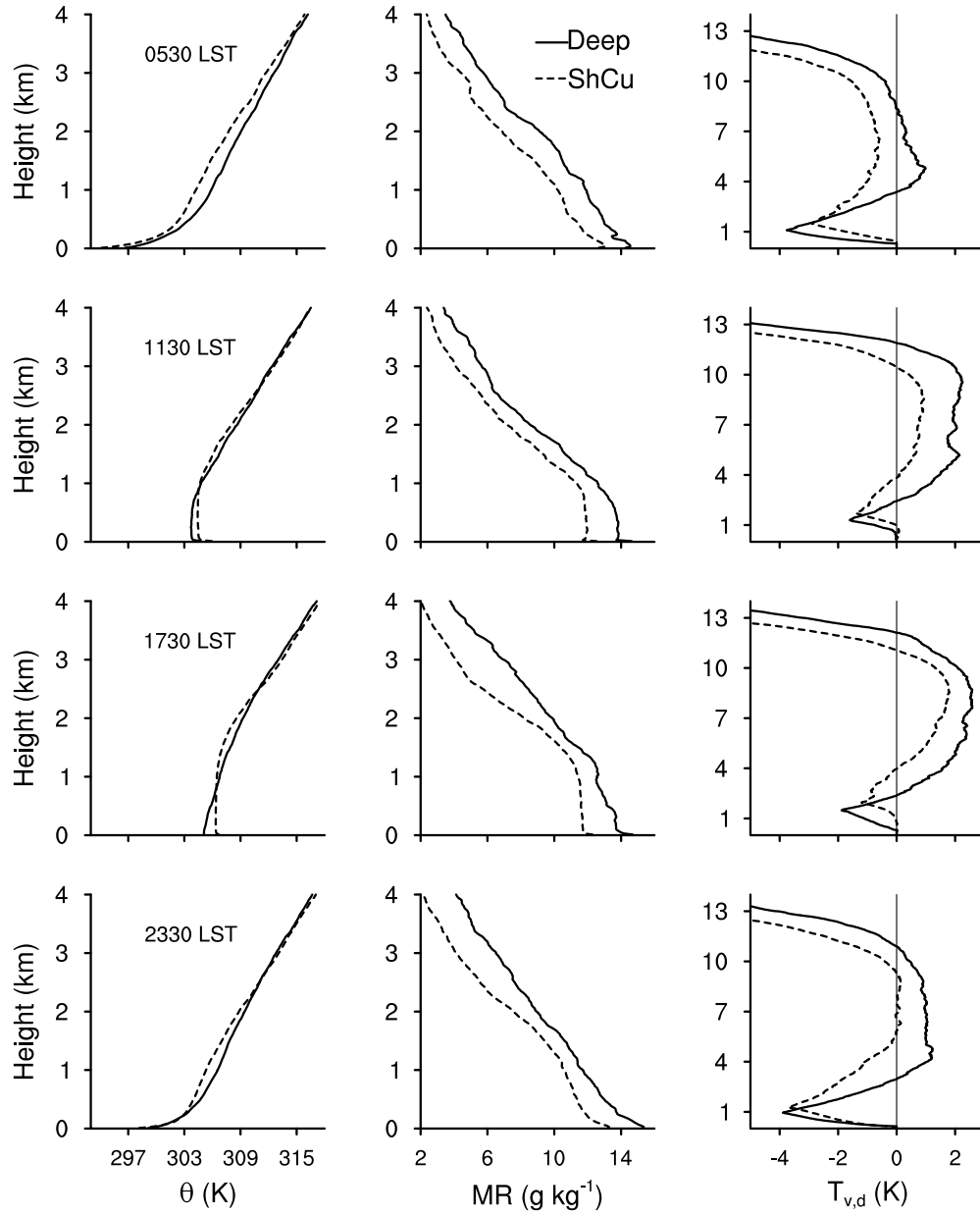


FIG. 4. Composite soundings for potential temperature (θ) and Mixing Ratio (MR) and the virtual temperature difference ($T_{v,d}$) between the environmental sounding and an air parcel lifted through reversible adiabatic processes from the boundary layer for fair-weather shallow cumulus days (dashed) and late-afternoon deep convection days (solid) at different Local Standard Times (LST).

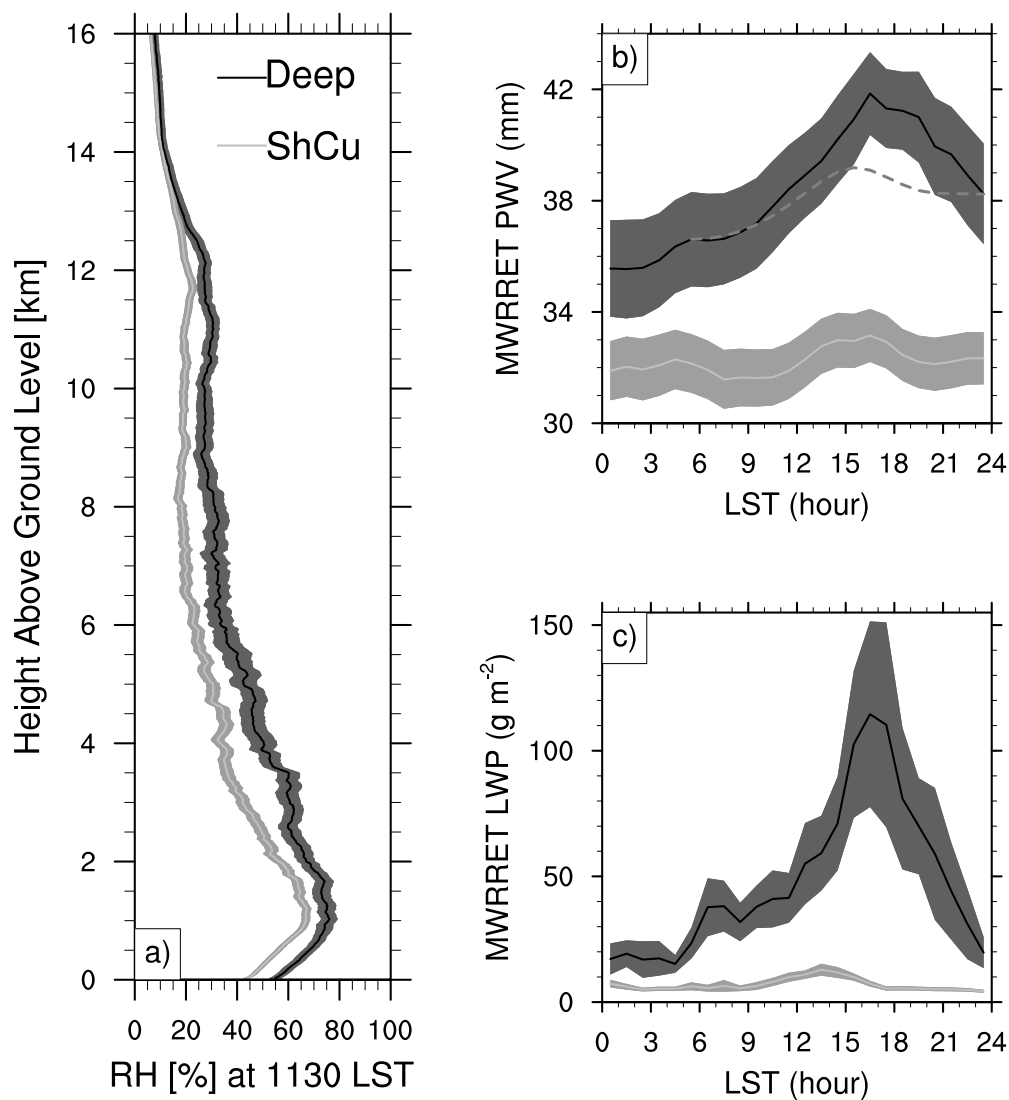


FIG. 5. Composite Relative Humidity (RH, a) at 1130 LST from sounding data and composite diurnal cycle of precipitable water vapor (PWV, b) and liquid water path (LWP, c) from CMBE MWRRET data. The width of the color shading on either side of the mean value denotes one standard error of the mean across all the sample days in each regime. The dashed line in panel b) is the PWV calculated based on the integral of evaporation and precipitation since 0530 LST for days with late-afternoon deep convection. Time-averaged LWP values are not conditioned on the presence of cloud and thus they are not in-cloud averages.

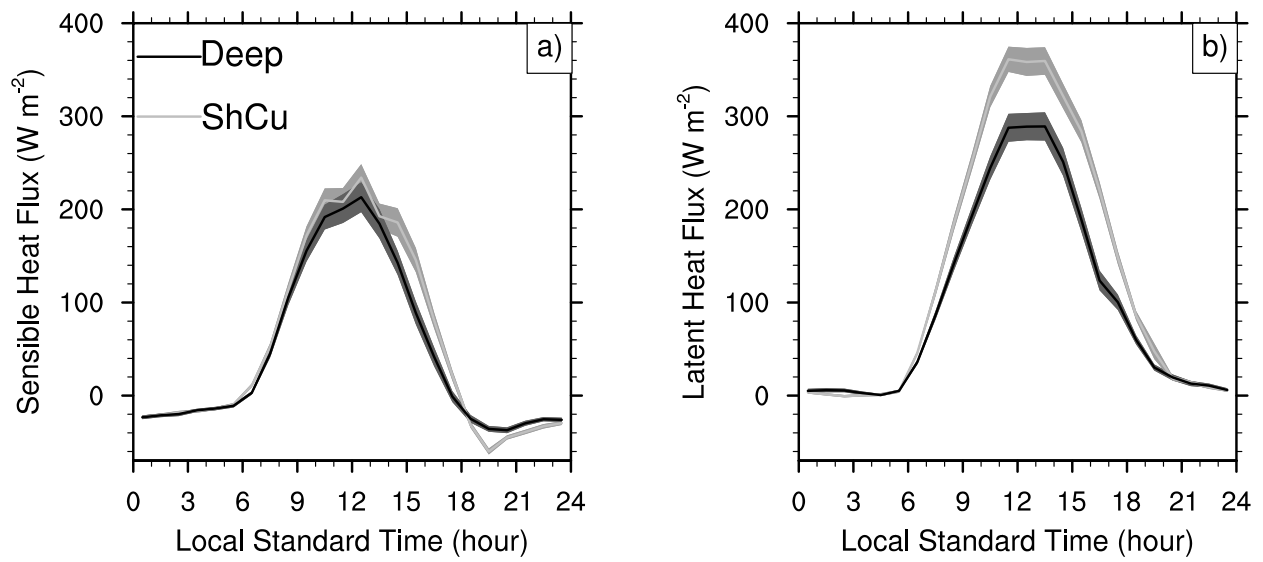


FIG. 6. Diurnal cycle composite of surface sensible heat flux (a) and latent heat flux (b) from BAEBBR data for fair-weather shallow cumulus days and late-afternoon deep convection days. The width of the color shading on either side of the mean value denotes one standard error of the mean across all the sample days in each regime.

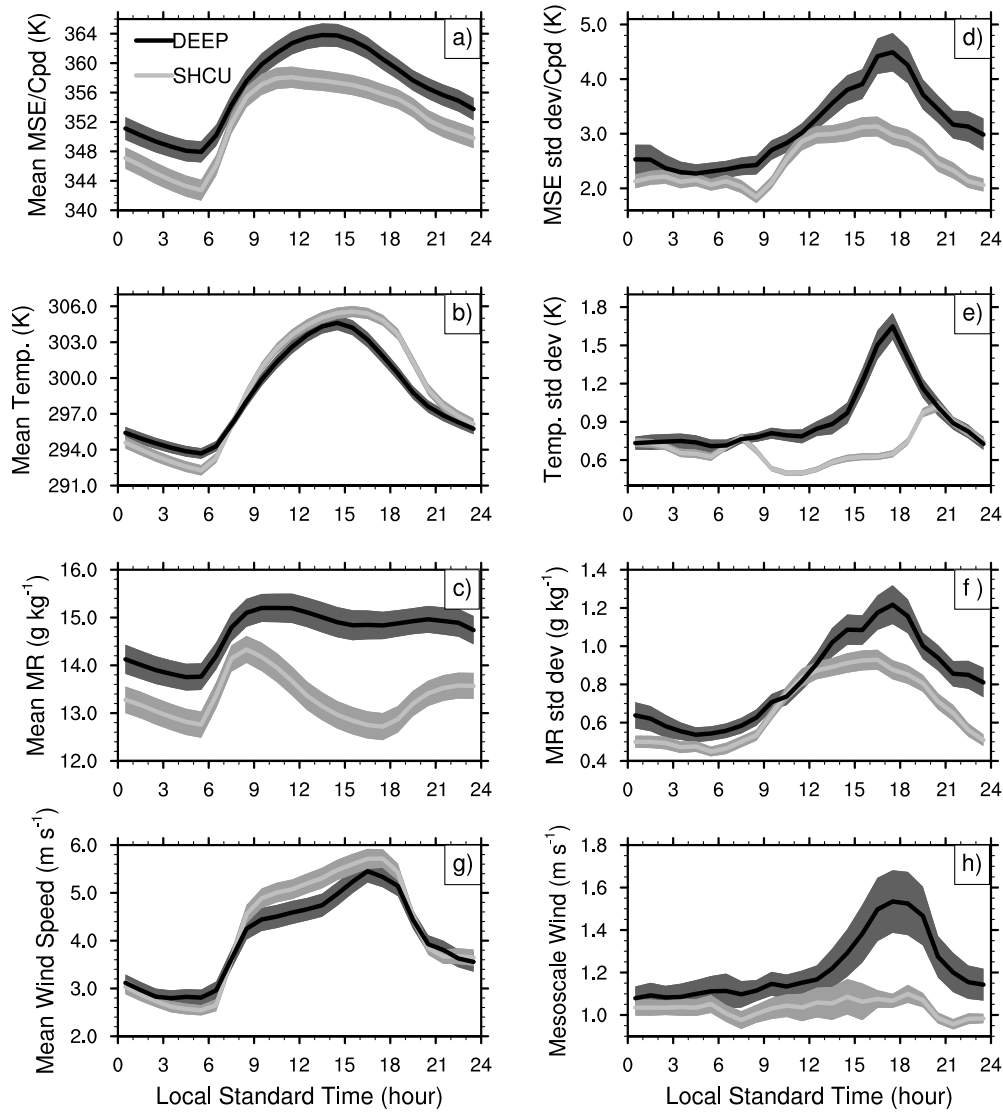


FIG. 7. Diurnal cycle composite of mean surface Moist Static Energy (MSE, a), temperature (b), and Mixing Ratio (MR, c), and their standard deviations (std dev, d-f). Also shown are the mean surface wind speed (g) and the mesoscale wind speed (h). Mean and std dev values are calculated based on SMOS data at the SGP central facility and four nearby Oklahoma Mesonet stations. Mean MSE and its std dev are normalized by the heat capacity at constant pressure for dry air (Cpd), and thus are in units of K. The width of the color shading on either side of the mean value denotes one standard error of the mean value across all sample days in each regime.

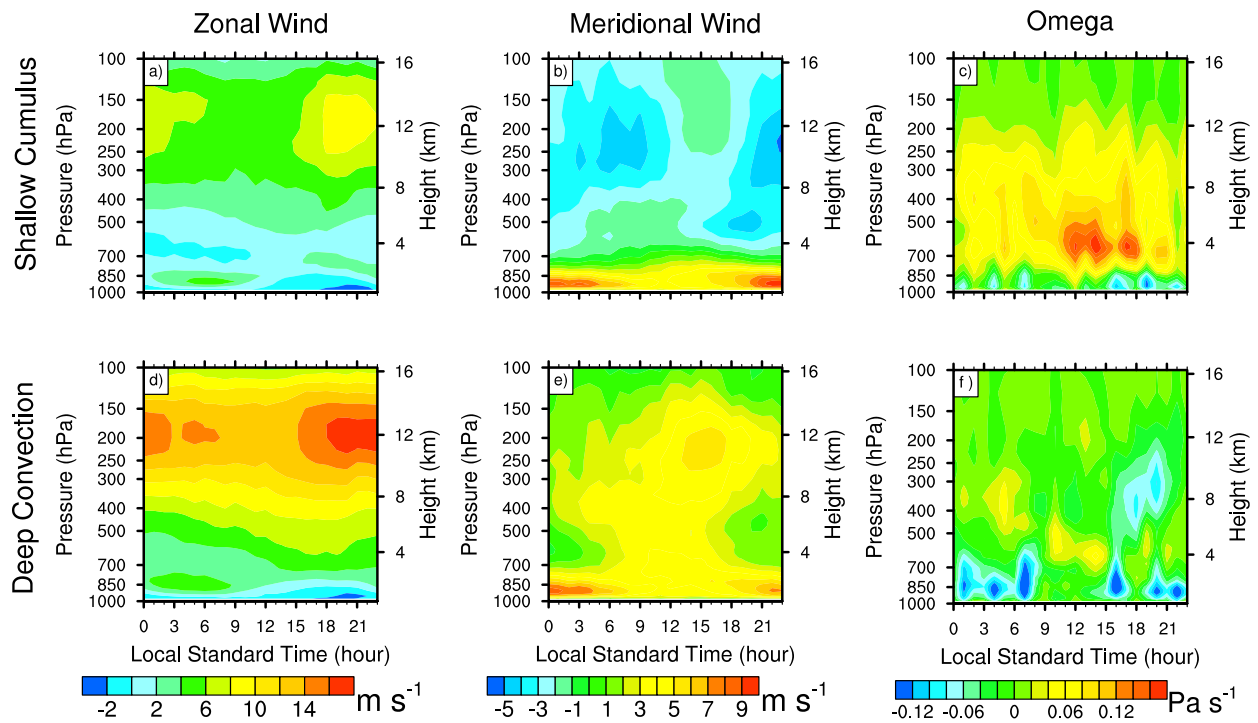
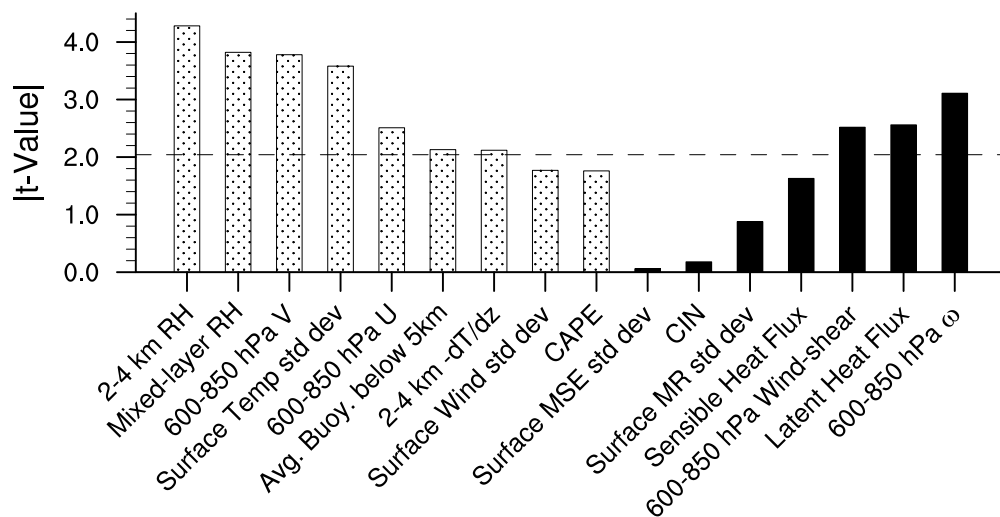


FIG. 8. Composite diurnal cycle of winds from the NCEP MOLTS data at SGP: zonal (left), meridional (middle) and vertical pressure wind (omega, right) for fair-weather shallow cumulus days (top) and late-afternoon deep convection days (bottom).



Environmental Parameters at 1130 LST

FIG. 9. Absolute t-values from student t-tests for the differences between composite means of fair-weather shallow cumulus days and late-afternoon deep convection days around 1130 LST. The horizontal line denotes a confidence level of 95%. Negative (positive) t-values are in solid (stipple) pattern, and denote smaller (larger) composite means on deep convection days relative to the mean on fair-weather shallow cumulus days.

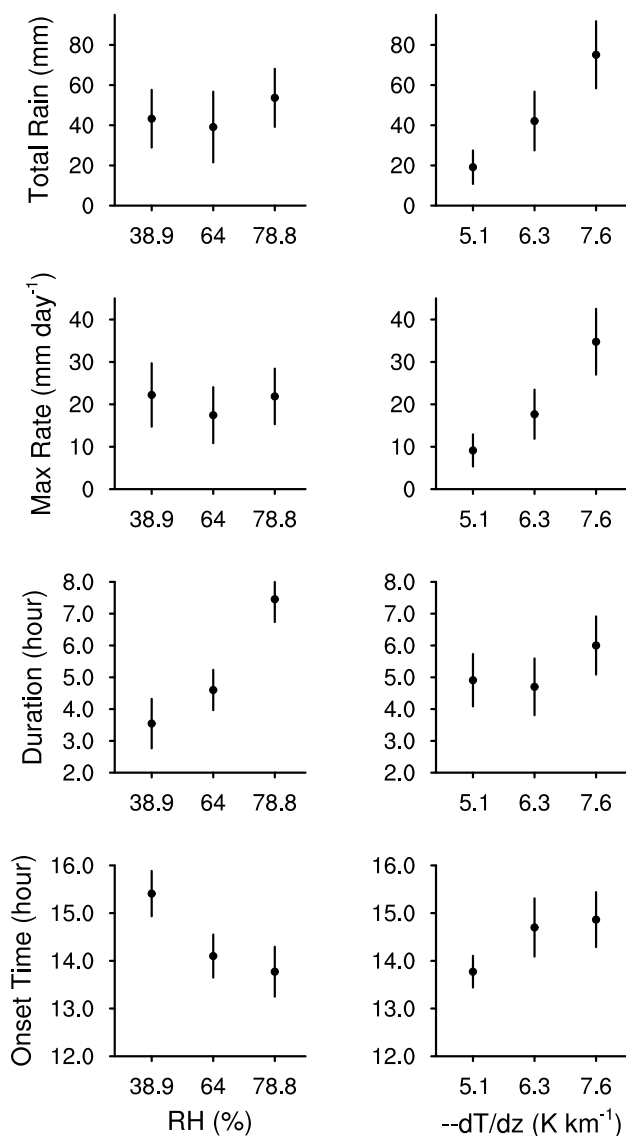


FIG. 10. Afternoon rain statistics stratified according to low, medium and high values of Relative Humidity (RH) and lapse rate ($-dT/dz$) between 2 and 4 km at 1130 LST. The statistics include total afternoon rain (top), maximum hourly rain rate (second), duration of rain event (third), and precipitation onset time (bottom). The black dots indicate the mean values of precipitation statistics and the width of the black lines indicate two standard errors. The mean values for each of the three ranges of RH and lapse rate are displayed on the abscissa.

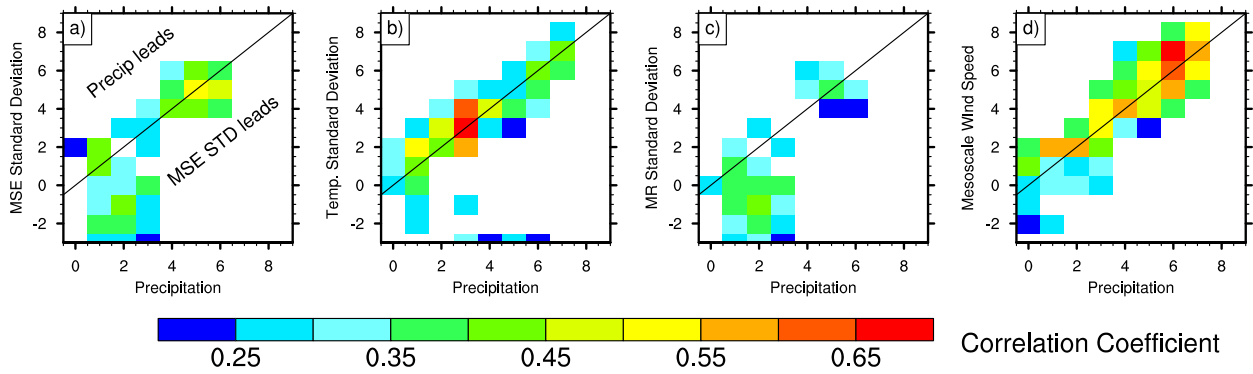


FIG. 11. Lead-lag correlation coefficients between the precipitation rate of late-afternoon deep convection days and the standard deviation of surface Moist Static Energy (MSE) (a), surface temperature (b), surface Mixing Ratio (MR) (c) and mesoscale wind speed (d). The scale for both the abscissa and ordinate are hours after precipitation onset time. Only correlation coefficients that are significant at 95% confidence level and have been calculated from samples sizes greater than 30 are displayed.

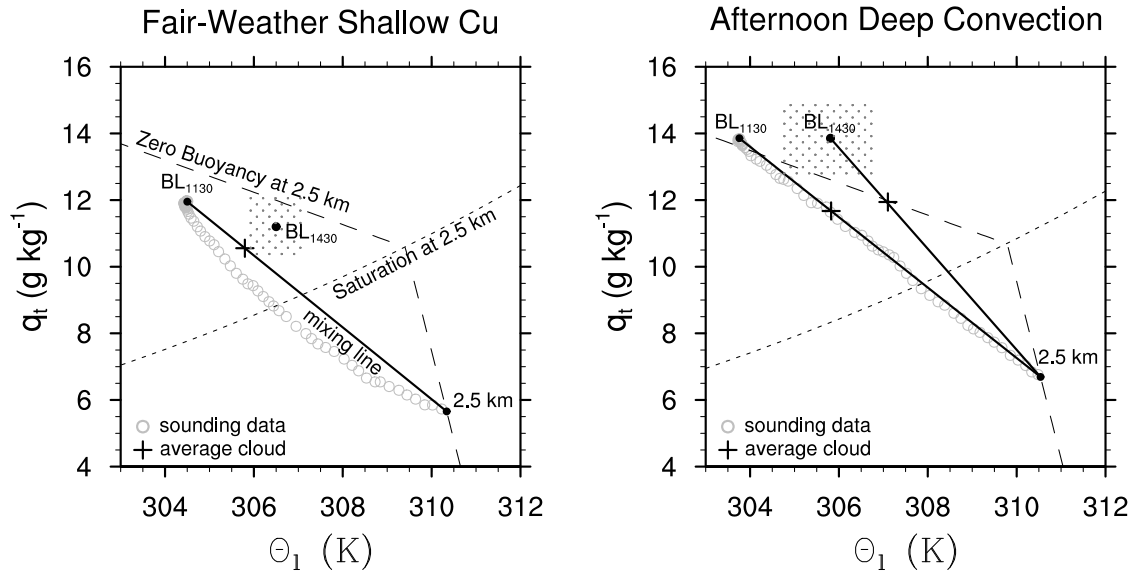


FIG. 12. Conservative variables diagram (Paluch diagram) of total water mixing ratio (q_t) and liquid water potential temperature (θ_l) for the composite of sounding data (gray circles) at 1130 LST for fair-weather shallow cumulus days (left) and late afternoon deep convection days (right). Dotted lines are the saturation curves and long-dashed lines are the zero-buoyancy lines calculated based on sounding data at 2.5 km. The black solid line connects the air properties in the boundary layer at 1130 LST (the black dot labeled “BL₁₁₃₀”) and at the level of 2.5 km (the black dot labeled “2.5 km”) and is the mixing line along which mixtures of air in boundary layer and the 2.5 km level would fall. The portion of the mixing line above the zero-buoyancy line indicates mixture is positively buoyant at 2.5 km. Above the saturation curve, the mixture is cloudy at 2.5 km. The black cross denotes the average property of the mixing line above the saturation curve which is an approximation to the average properties of the cloud at 2.5 km. The boundary layer air property at 1430 LST is denoted by black dot labeled “BL₁₄₃₀”. The stippled area denotes the possible values a boundary layer air parcel may have if boundary layer inhomogeneity is considered. This area encompasses one standard deviation of boundary layer inhomogeneity about the mean value (Figure 7).

List of Tables

1	Correlation coefficients between environmental parameters at 1130 LST and afternoon rain statistics. Correlation coefficients are shown only if the relationship is significant at the 95% confidence level.	46
---	--	----

	Total Rain	Max Rain rate	Onset Time	Duration
CAPE			0.414	-0.417
CIN				
Average Buoyancy below 5 km				
2-4 km $-dT/dZ$	0.496	0.518		
2-4 km RH			-0.395	0.464
Mixed-Layer RH				
Surface Moist Static Energy std dev	0.437	0.513		
Surface Mixing Ratio std dev	0.443	0.492		
Surface Temperature std dev	0.550	0.552		
Surface Mesoscale Wind	0.514	0.486		
Sensible Heat Flux				
Latent Heat Flux				-0.436
600-850 hPa Wind-shear				
600-850 hPa ω				
600-850 hPa U	0.454	0.549		
600-850 hPa V				

TABLE 1. Correlation coefficients between environmental parameters at 1130 LST and afternoon rain statistics. Correlation coefficients are shown only if the relationship is significant at the 95% confidence level.